Science of the Total Environment 995 (2025) 180088

Contents lists available at ScienceDirect

Science of the Total Environment

journal homepage: www.elsevier.com/locate/scitotenv

Coupling global climate drivers to dust emission dynamics at Etosha Pan, Namibia

Natasha S. Wallum [a,*], Giles F.S. Wiggs [a], Robert G. Bryant [b]

[a] School of Geography and the Environment, Oxford University Centre for the Environment, University of Oxford, United Kingdom
[b] School of Geography and Planning, University of Sheffield, United Kingdom

HIGHLIGHTS

- A 22-year record shows dust emission at Etosha Pan is driven by the timing and extent of precipitation and flooding events.
- Dust emissions peak in dry years where wind strength acts as the dominant control on dust emission activity.
- Pan flooding and precipitation suppress dust in wet years but can enhance emissions after drying over ~3-month seasonal timescales.
- Increased dust emissions are associated with positive ENSO and negative SIOD phases.

GRAPHICAL ABSTRACT

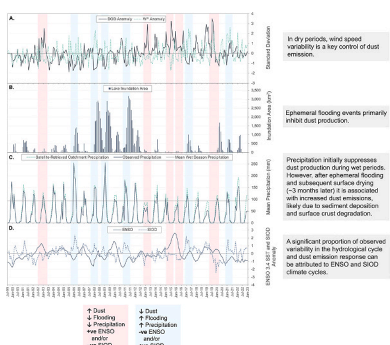

ARTICLE INFO

Keywords:
Dust
Climate
Hydrology
Etosha Pan
Namibia

ABSTRACT

Ephemeral lake beds are globally significant sources of atmospheric mineral dust aerosols, but emissions from these topographic features are characterised by considerable spatial and temporal variability. Resolving the complex relationships between climatic and surface drivers that control aeolian emissivity has proven extremely challenging, leading to substantial uncertainty in model predictions of atmospheric dust loading and its impacts on other global-scale Earth system processes. This study uses a range of satellite-derived measurements (e.g., MSG-SEVIRI, MODIS) of mineral dust aerosols, lake inundation, catchment precipitation, and climate data (from meteorological stations and model reanalysis data sources) from 2000 to 2022 to assess the influence of regional climate and basin-scale hydrology on the emission of mineral dust from Etosha Pan in Namibia, a major Southern Hemisphere dust source. Significant associations were identified between interannual and seasonal variations in catchment rainfall, ephemeral pan surface inundation, and the frequency and magnitude of dust emissions over the two-decade analysis period. Results indicate that dust production is modulated by seasonal precipitation and ephemeral flooding events, which suppress dust emissions during wet periods and also lead to the delayed production of dust emissions on surface drying. During dry periods, wind speed variability was identified as the primary driver of dust emissions. These regional climate and hydrological factors were found to be closely linked to El Niño-Southern Oscillation (ENSO) phases and shifts in the subtropical Indian Ocean Dipole (SIOD), where seasonal increases (reductions) in dust emissions were associated with positive (negative) ENSO and negative (positive) SIOD events. The identification of robust links between dust emissions and global climate drivers in

* Corresponding author.
E-mail address: natasha.wallum@ouce.ox.ac.uk (N.S. Wallum).

https://doi.org/10.1016/j.scitotenv.2025.180088
Received 9 April 2025; Received in revised form 8 July 2025; Accepted 13 July 2025
Available online 18 July 2025

this study makes a significant contribution to the improved integration of ephemeral lake systems in dust emission models and opens the potential for forecasting future dust trends based on large-scale climate cycles.

1. Introduction

Windblown mineral dust from desert regions plays a critical role in the Earth's land-atmosphere-ocean-biosphere system. Dust influences a range of processes, including climate regulation (Kok et al., 2018, 2023), ocean fertilisation (Dansie et al., 2022; Meng et al., 2022), nutrient cycling (Mahowald et al., 2008; Kumar et al., 2022), and air quality with implications for human health (Prospero et al., 2021; Tong et al., 2023). The accurate representation of major dust source regions in global climate models (GCMs) is therefore essential to simulate the spatiotemporal dynamics of the atmospheric dust cycle and its interactions with other components of the Earth system, particularly under climate and land-use change scenarios (Zhao et al., 2022).

Remote sensing studies have identified ephemeral lake beds in their dry phases (pans or playas) as regionally and globally significant dust sources (Prospero et al., 2002). These flat, intermittently flooded, and often salt-crusted surfaces are found in topographic lows of endorheic basins where evaporation exceeds water input. Cycles of flooding and desiccation regulate the accumulation and exposure of fine-grained alluvial sediments and evaporite minerals, modulating both the supply of erodible material and the surface conditions that control dust emissivity (González-Romero et al., 2024). Despite growing recognition of the importance of ephemeral lake beds in global dust budgets, major uncertainties persist in representing the magnitude and variability of dust emissions from these features in numerical dust models (Banks et al., 2022; Chappell et al., 2023). These limitations are largely due to an incomplete understanding of the interactions between regional climate variability, catchment-scale hydrology and surface erodibility factors, such as soil moisture and crust formation (Reynolds et al., 2007, 2009).

Among these globally significant ephemeral lake systems, Etosha Pan in northern Namibia is a particularly prominent and climatically sensitive dust source region (Clements and Washington, 2021, 2023; Wiggs et al., 2022). Situated within the endorheic Cuvelai-Etosha Basin, the pan undergoes recurrent cycles of inundation and desiccation that influence sediment surface properties and dust emission potential (Bryant, 2003; Mahowald et al., 2003; Mendelsohn et al., 2013). These dynamic surface conditions, coupled with frequent exposure of fine-grained salt-rich deposits, make Etosha Pan one of the most active dust sources in the Southern Hemisphere (Prospero et al., 2002; Washington et al., 2003; Vickery et al., 2013). Yet to date, no comprehensive study has linked long-term rainfall variability, lake bed hydrology, and global climate cycles to the spatiotemporal dynamics of dust emissions from Etosha Pan. Previous work in the region has established that precipitation and pan surface flooding are highly variable (Mendelsohn et al., 2013; Hamunyela et al., 2022), and that rainfall patterns in southern Africa are influenced by El Niño-Southern Oscillation (ENSO) phases and related sea surface temperature (SST) anomalies in the Indian and South Atlantic Oceans (Reason and Rouault, 2002; Bryant et al., 2007; Gaughan et al., 2016). However, these large-scale climate drivers have not yet been explicitly connected to dust emissions through a hydrologically and meteorologically integrated framework. Early remote sensing work using AVHRR and TOMS satellite datasets provided preliminary evidence that ephemeral flooding events suppressed dust activity for several months following inundation, but also suggested a delayed increase in dust emissions 1–2 years after such events (Bryant, 2003; Mahowald et al. (2003). However, these studies were constrained by sparse event records and a short observation period ($<$3 inundation events across $<$10 years), limiting their explanatory power (Bryant et al., 2007).

This study addresses this knowledge gap by integrating extended time-series of climate and remote sensing data to assess the hydrological and meteorological controls on aeolian dust emissions from Etosha Pan, Namibia, over a 22-year period (2000–2022). Specifically, we pursue four objectives: (1) to characterise the spatiotemporal dynamics of mineral dust emissions using multi-sensor (MSG-SEVIRI and MODIS) satellite-based dust plume detection and dust optical depth (DOD) measurements; (2) to determine the meteorological contexts for observed dust activity using ERA5-Land near-surface wind data; (3) to assess the relationship between dust emissions, catchment-scale precipitation (from GPM-IMERG, TRMM and meteorological station records) and pan surface inundation (from MODIS reflectance data); and (4) to evaluate the influence of large-scale climate oscillations and SST anomalies on hydrological variability and dust activity from this key source region. By clarifying the interplay between regional hydrology, surface conditions, and large-scale climate drivers, this study provides new insights into the mechanisms controlling dust emissions from ephemeral lake systems and supports improved representation of these processes in global dust and climate models.

2. Study area

Etosha Pan is a 4800 km^2 endorheic basin that forms the terminus of the Cuvelai-Etosha drainage system, which spans approximately 130,000 km^2 across southern Angola and northern Namibia (Fig. 1) (Mendelsohn et al., 2013). Seasonal rainfall during the austral summer months (November to April) drives an ephemeral drainage system to the north of Etosha. This system comprises a broad network of ephemeral channels, locally termed *iishana* (plural) or *oshana* (singular), which converge into the Ekuma River and drain into the northwestern part of Etosha Pan. Additional inflows occasionally originate from the Oshigambo, Oshangulu and Owambo Rivers, entering the northern and eastern margins of the pan (Fig. 1a) (Hamunyela et al., 2022). These ephemeral river systems are believed to supply fine-grained fluvial sediments to Etosha Pan during intermittent periods of shallow inundation (Fig. 1b) (Bryant, 2003; Mahowald et al., 2003).

During the dry austral winter months (May to October), the groundwater table lowers, exposing the surface of the pan. This surface is rich in fine clay and silt-sized sediments attributed to the Andoni Formation (Pickford et al., 2009), along with extensive evaporite (salt) deposits (Buch and Rose, 1996; Rahm and Buch, 1997; Li et al., 2018). Due to the dry conditions and extreme salinity, the pan is largely devoid of vegetation. As a result, the bare surface is highly susceptible to erosion by the predominant E-NE regional winds, often leading to significant dust emission events (Fig. 1c) (Clements and Washington, 2021, 2023; Wiggs et al., 2022).

3. Methods

3.1. Dust event detection and mineral aerosol data

To assess the spatiotemporal dynamics of dust emissions from Etosha Pan and determine the potential relationships with regional hydrology, ephemeral surface inundation, and wind erosivity, we employed a multi-sensor satellite remote sensing approach using MSG-SEVIRI and MODIS data for the period 2000–2022.

The Spinning Enhanced Visible and InfraRed Imager aboard Meteosat's Second Generation satellites (MSG-SEVIRI; available since 2005) served as the primary data source for detecting and characterising dust emission events due to its high temporal resolution (15-min intervals) and moderate spatial resolution (3 km) (Vickery et al., 2013). Level 1.5 MSG-SEVIRI imagery for the period 2005–2022 were obtained from the EUMETSAT Data Store (https://data.eumetsat.int/search?quer y=).

Dust plume detection was performed using the 'clear sky' differencing (CSD) multi-temporal analysis technique (Murray et al., 2016). The CSD background reduction algorithm builds upon the widely used Dust RGB scheme (Lensky and Rosenfeld, 2008) by removing surface reflectance and thermal emission features associated with the underlying surface and atmospheric conditions to enhance dust signals in MSG-SEVIRI false-colour imagery. This technique improves discrimination between dust and meteorological clouds or bright land surfaces and enhances source identification under varying conditions, including low dust concentrations or mineralogical variability (e.g., high salt or low quartz content). A detailed description of the process applied to yield clear sky difference (CSD) images from MSG-SEVIRI time-series data is given in Murray et al. (2016). CSD images were rendered at hourly time-steps (day and night) across all seasons from 2005 to 2022.

Given the lack of a single long-term remote sensing product capable of consistently detecting regional dust source activity, we supplemented MSG-SEVIRI data with imagery from the Moderate Resolution Imaging Spectroradiometer (MODIS) aboard the Terra and Aqua satellites. MODIS Surface Reflectance products (MOD09GA/MYD09GA; bands 1–7) at 500 m resolution were obtained for 2000–2022 from NASA's LAADS DAAC (https://ladsweb.modaps.eosdis.nasa.gov/) for satellite overpass times ~1030 UTC (Terra) and ~1330 UTC (Aqua), bridging the 2000–2005 gap in MSG-SEVIRI coverage and ensuring continuity in dust event monitoring over the entire analysis period. We acknowledge that the twice-daily observations of MODIS may miss short-term dust events due to relatively infrequent overpasses, resulting in detection biases (Ginoux et al., 2010). However, this limitation primarily applies to the early years of the study (2000–2004), when MODIS was the sole data source due to the absence of MSG-SEVIRI coverage. To mitigate this, we leveraged the complementary strengths of both MODIS and MSG-SEVIRI: the higher spatial resolution of MODIS (500 m) enabled the identification of smaller dust plumes missed by MSG-SEVIRI, while the higher temporal resolution of MSG-SEVIRI CSD composites (hourly data) provided more frequent monitoring, ensuring that dust events occurring outside of MODIS's observation windows were captured for the majority of the study period. By combining these datasets, we compensated for both the temporal gaps in MODIS coverage during the early years and the spatial limitations of MSG-SEVIRI, resulting in a more complete and consistent record of dust plume activity. Visual interpretation of the MSG-SEVIRI CSD and MODIS true-colour (bands 1, 4, and 3) composites enabled the identification of dust plume initiation points and associated metrics (e.g., uplift timing, direction, and duration). These data were then compiled into a GIS database of spatially-referenced vector points.

To estimate the magnitude of dust emissions, we used MODIS Level 2 Deep Blue aerosol products (MOD04_L2/MYD04_L2), which provide measurements of the aerosol optical depth (AOD) at 0.55 μm and other aerosol properties (e.g., Ångström exponent and single scattering albedo) at 10 km resolution up to twice-daily. The Deep Blue algorithm is optimised for bright surfaces, such as arid regions (Hsu et al., 2004, 2013) and enables extraction of dust optical depth (DOD) by isolating the mineral dust component from total AOD (Ginoux et al., 2010, 2012; Pu and Ginoux, 2016).

To distinguish dust from non-dust aerosols (primarily smoke aerosols from biomass burning in surrounding areas and sea spray aerosols from the coast) we applied thresholds to the Ångström exponent (AE) and single scattering albedo (SSA). We used a threshold of AE < 0.6 to filter out biomass smoke (Schepanski et al., 2007). This threshold was selected following preliminary analyses comparing multiple AE constraints, which showed that AE < 0.6 consistently minimised the influence of biomass-burning aerosols while preserving mineral dust signals originating from Etosha Pan. To exclude sea salt aerosols, a threshold of SSA < 1 at 0.47 μm was applied (Ginoux et al., 2012). This yielded a daily time-series of DOD values representing mineral dust loading attributable to emissions from Etosha Pan.

Daily, monthly and annual dust event frequencies were compiled from identified plume records and compared with corresponding dust aerosol optical depth (DOD) data to assess temporal patterns in dust event frequency and magnitude, including their seasonal and inter-annual variability, across the 2000–2022 analysis period.

3.2. Meteorological context for dust event detection

To determine if the observed dust emissions from Etosha Pan were associated with meteorological conditions, detected dust plume events and dust days (i.e., days that dust plumes were observed emitting from the pan surface) were evaluated against near-surface wind regimes

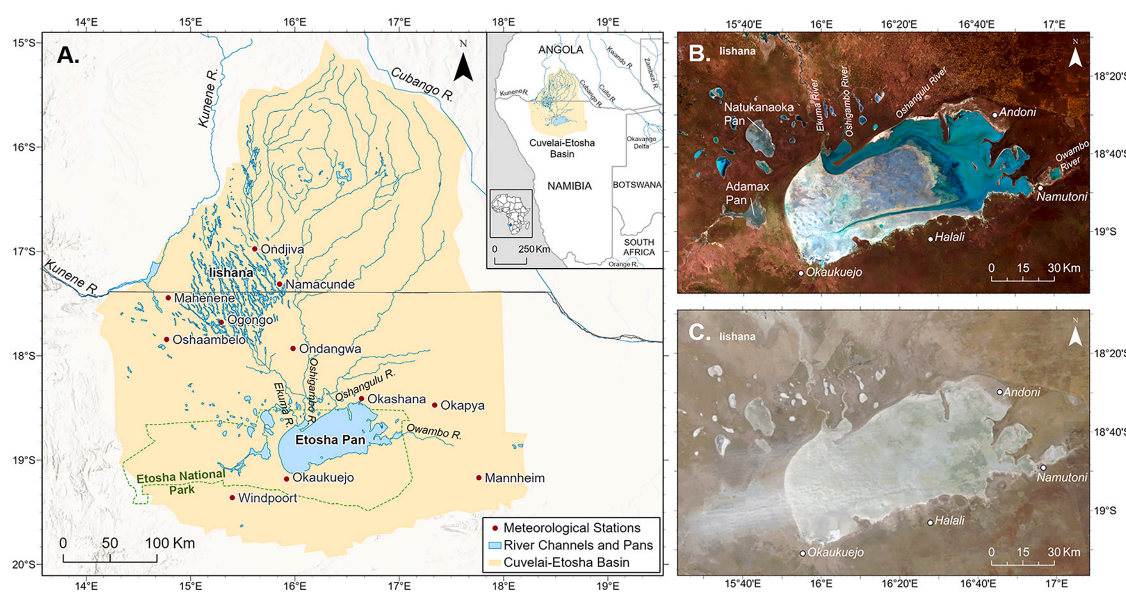

Fig. 1. The geographic location of Etosha Pan within the Cuvelai-Etosha Basin in Namibia, highlighting (a) key river networks and the principal meteorological stations used in this study. Figure insets display (b) a Landsat 8 OLI false colour composite (bands 7, 4, 1) image captured on 7 May 2020 showing ephemeral flooding of Etosha Pan and key hydrological features, and (c) a MODIS Terra true colour composite (bands 1, 4, 3) image captured on 7 September 2019 1030 UTC showing a dust emission event blowing towards the west.

derived from ERA5-Land (10 m wind speed and wind gusts) reanalysis data (Muñoz-Sabater et al., 2021), which has been established as a valid representation of local atmospheric conditions at Etosha Pan (Gadal et al., 2022). Hourly estimates of wind conditions (10 m horizontal [u] and vertical [v] components and wind gusts) at Etosha Pan for the period 2000–2022 were derived from ERA5-Land reanalysis available from the Copernicus Climate Change Service Data Store (https://cds.climate.copernicus.eu/). Calculated u and v vector components were corrected with relevant off-set and scaling factors, from which wind speeds (m s^{-1}) and direction (°) were computed. Wind gusts (m s^{-1}) were defined as the maximum 10 m wind speed computed for each hourly timestep.

3.3. Surface hydrology

To investigate the relationship between regional precipitation, pan surface flooding, and dust emission dynamics, statistical analyses (Pearson correlation) were performed across daily, monthly and annual timescales over the 2000–2022 analysis period.

Surface inundation data were derived from daily MODIS Terra (500 m spatial resolution) imagery using a dynamic density thresholding technique (Bryant and Rainey, 2002) applied to near-infrared (NIR) reflectance values (MODIS band 2; 0.84–0.88 μm). This method generated a time-series of 7594 daily surface flooding records, capturing surface water extents (km^2 and % of total pan area) from 2000 to 2022.

Daily precipitation inputs across the Cuvelai-Etosha Basin (July–June hydrological year) were derived from the Tropical Rainfall Measuring Mission (TRMM) (1999–2000) and the Integrated Multi-Satellite Retrievals for GPM (GPM-IMERG) (2000–2022) gridded precipitation datasets, with spatial resolutions of 0.25° × 0.25° and 0.1° × 0.1°, respectively. These data were obtained from the Goddard Earth Sciences Data and Information Services Center (http://disc.gsfc.nasa.gov/). At the approximate latitude of the Cuvelai-Etosha Basin (~18°S), these resolutions correspond to grid cells of ~27.75 km × 26.5 km for TRMM and ~11.1 km × 10.6 km for GPM-IMERG. These grid sizes are comparable to, or finer than, those typically used in regional and global dust emission models (Zhao et al., 2022) and are suitable for capturing mesoscale convective systems and large storm cells, which are key drivers of hydrological and dust-related dynamics in the region (Clements and Washington, 2021; Wiggs et al., 2022). The TRMM and GPM-IMERG datasets were selected based on their demonstrated ability to provide robust and accurate precipitation estimates in semi-arid, data-scarce regions such as southern Africa (Pradhan et al., 2022). Compared to other satellite-derived data products (e.g., CHIRPS) and reanalysis datasets, TRMM and GPM-IMERG exhibit superior spatial and temporal fidelity, lower bias, and stronger correlation with in-situ rainfall observations (Peng et al., 2021). Their compatibility and continuity also support consistent analysis over the full 22-year study period, a crucial advantage over datasets with limited historical coverage or coarser temporal resolution. To further validate and enhance these satellite-derived estimates, we integrated monthly precipitation totals (2000–2022) from ten regional weather stations provided by the Southern African Science Service Centre for Climate Change and Adaptive Land Management (SASSCAL) (https://sasscal.org/), as well as continuous rain gauge records from Windpoort, located within the basin (Fig. 1).

To explore links between inter-annual rainfall variability in the Cuvelai-Etosha Basin and global climate cycles, Pearson correlation analyses were performed using various climate indices: the Tropical Pacific El Niño-Southern Oscillation SST anomalies in the Niño 3.4 region (ENSO 3.4), the Subtropical Indian Ocean Dipole Index (SIOD), SST anomalies from the western and eastern Indian Ocean (West IO and East IO), the Tropical Southern Atlantic Index (TSA), the Multivariate El Niño-Southern Oscillation Index (MEI V2), and the Dipole Mode Index (DMI). Time-series of standardised quarterly rainfall anomalies (DJF, MAM, JJA, SON) from 2000 to 2022 were extracted from the satellite-derived gridded precipitation datasets. SST anomaly data were sourced from the Climate Diagnostics Centre (CDC) online archives (http://psl.noaa.gov/data/climateindices) and the IOD data from the Frontier Research System for Global Change (FRSGC)/Japan Agency for Marine-Earth Science and Technology (JAMSTEC) (http://www.jamstec.go.jp).

4. Results and discussion

4.1. Mineral dust emissions

4.1.1. Annual trends

The inter-annual variations in dust optical depth (DOD) values and number of dust plume events and associated dust days (i.e., days that dust plumes were observed emitting from the pan surface) derived from MSG-SEVIRI and MODIS satellite data are displayed in Fig. 2. A total of 785 dust plumes were detected from Etosha Pan over the course of 428 days in the 2000–2022 analysis period, with dust plumes observed emanating from Etosha Pan every year. The total number of plumes detected each year was generally greater than the total number of observed dust days (Fig. 2), indicating that several individual plume events were detected in a single dust day.

Both elevations in mean annual DOD values and the highest number of dust plume events and dust day occurrences were recorded in 2015 (mean DOD: 0.17 ± 0.08; 138 dust plumes within 74 dust days), 2016 (mean DOD: 0.14 ± 0.08; 116 dust plumes within 64 dust days), and 2019 (mean DOD: 0.18 ± 0.09; 107 dust plumes within 54 dust days) (Fig. 2). However, elevations in mean DOD values were not always synonymous with the annual number of dust plume events and dust days. For example, elevations in dust optical depth values were observed in 2013 (mean DOD: 0.11 ± 0.03) despite the relative infrequency of observed dust emissions (8 dust plumes within 8 dust days) (Fig. 2). This apparent discrepancy likely reflects the presence of advected mineral dust from smaller pans and ephemeral river channels (iishana) surrounding Etosha Pan under dry conditions, as previously noted by Bryant (2003). While these smaller sources contributed to a certain extent to local-scale dust loading, their emissions were relatively minor and often coincided with more widespread dusty conditions, rather than representing distinct, large-scale events. Further research is needed to better quantify the contribution of these secondary sources and fully characterise the dust load from the Etosha region.

4.1.2. Seasonal cycle

Fig. 3 illustrates the seasonality associated with mean monthly DOD values, plume events, and dust day occurrences at Etosha Pan from 2000 to 2022. While dust emission activity occurred in the region throughout the annual cycle, the satellite-observed dust event frequencies suggest that austral winter (May–October) emission events occurred more frequently (721 dust plumes within 388 dust days) than austral summer (November–April) events (64 dust plumes within 40 dust days) for the analysis period (Fig. 3), corresponding to findings from previous remote sensing studies in the region (Mahowald et al., 2003; Bryant et al., 2007; Vickery et al., 2013; Murray et al., 2016; Wiggs et al., 2022). However, it is well established that satellite retrievals are subject to biases, particularly in detecting shallow dust layers, dust over bright surfaces, and dust beneath cloud cover (Banks et al., 2022). Importantly, many dust plumes associated with cold pool outflow events in the austral summer were likely obscured by convective storm clouds in the remote sensing imagery, contributing to an underestimation of summertime emissions in this study. An observation which confirms the inherent underestimation by satellite remote sensing studies of the smaller but not insignificant contribution of austral summertime emissions to the annual dust loading cycle of Etosha Pan (Clements and Washington, 2023).

The seasonal trends observed in this study align with findings by Wiggs et al. (2022) that compared dust event frequencies with field-based dust flux measurements from July 2015 to July 2016. While their analysis confirmed that dust emissions occur throughout the year,

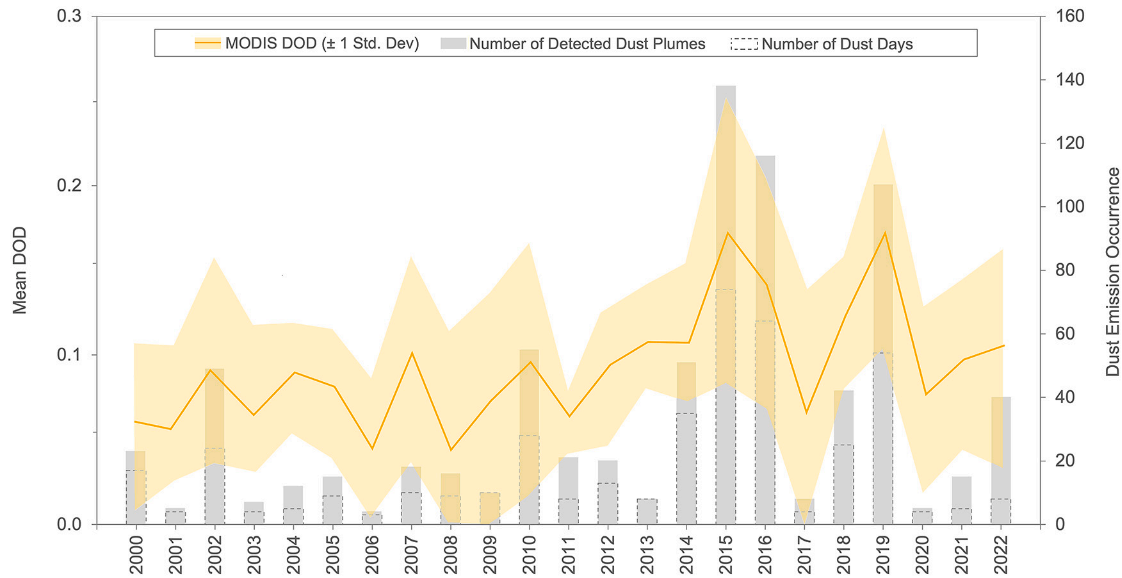

Fig. 2. Annual values of mean daily dust aerosol optical depth (DOD) and total number of dust plume events and dust days at Etosha Pan from 2000 to 2022.

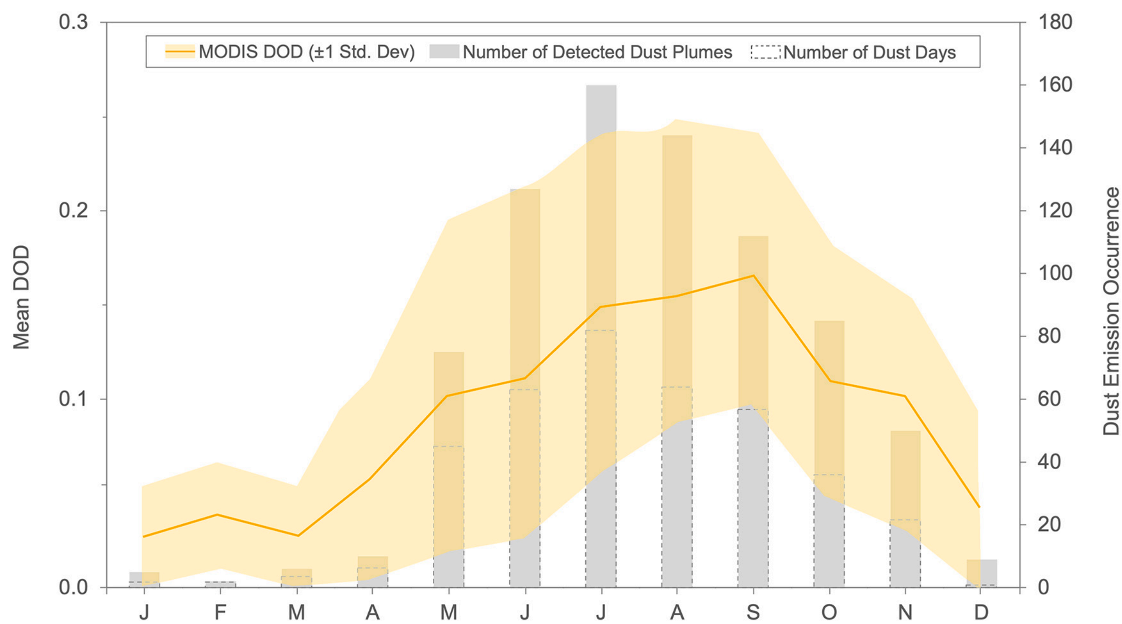

Fig. 3. Monthly values of mean daily dust aerosol optical depth (DOD) and total number of dust plume events and dust days at Etosha Pan from 2000 to 2022.

field data showed that the magnitude of dust emissions, in terms of flux, peaked in the spring. This indicates that remote sensing effectively captures seasonal variations in dust event frequency but may underestimate the actual dust flux, particularly during summer when fewer but potentially more intense dust events occur. Such discrepancies highlight the importance of integrating remote sensing with in-situ field measurements to achieve a more comprehensive understanding of both the timing and magnitude of aeolian dust emissions from desert playa sources.

4.2. Meteorological context for dust emissions

Records of plume events detected from the hourly MSG-SEVIRI CSD time-series data from 2000 to 2022 (Fig. 4) revealed that the majority (96 %) of dust events were observed in the early morning hours between 0500 and 0900 UTC (peak frequency at 0700–0800 UTC). However, a smaller proportion (4 %) of dust events were observed in the mid-morning between 1000 and 1100 UTC and afternoon to late evening hours between 1200 and 2200 UTC. The morning dust events were typically longer in duration (lasting anywhere between 30 and 550 min) compared to the relatively short-lived (restricted to durations of 30 to 120 min) afternoon/evening events (Fig. 4). This corresponds with field-based observational data from Etosha Pan (Clements and Washington, 2021; Wiggs et al., 2022), in which the general distinction between earlier (longer) dust emission events and later (shorter) dust emission events have been associated with two contrasting climatological mechanisms driving dust dynamics in this region during different seasons; the breakdown of low-level jets (LLJ) in the morning during the austral winter months and cold pool outflows (CPO) associated with convective storms in the late afternoon and evening during the austral summer.

To resolve the erosivity conditions associated with observed dust

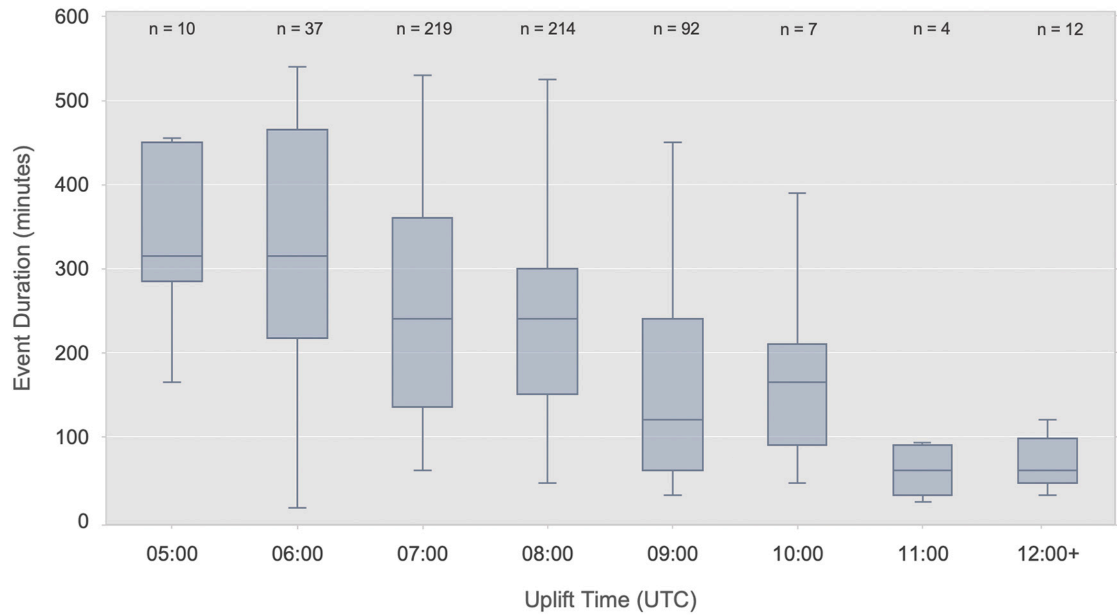

Fig. 4. Box and whisker plots showing dust events detected from MSG-SEVIRI clear sky differencing (CSD) time-series discriminated by measured time of uplift (UTC) and event duration (defined as the time in minutes between the measured time of uplift at-source and when the connection between the plume tail and source becomes detached).

emissions from Etosha Pan, detected dust events were evaluated against near-surface wind regimes derived from ERA5-Land (10 m wind speed and wind gusts) reanalysis data. Fig. 5 shows the frequency of dust plume events observed in 2000–2022 compared to the 10 m wind speeds and directions for the corresponding time and location of initial uplift. Results indicate a clear directional predominance in dust plume development from Etosha Pan, where the majority of dust emission events were initiated by strong winds exceeding 6 m s^{-1} originating from the E–NE (60°–80°) (Fig. 5). Data here concur with previous studies which have shown that dust emissions from Etosha Pan are associated with E–NE winds exceeding erosive threshold speeds of c. >6 m s^{-1} (Vickery et al., 2013; Murray et al., 2016; Wiggs et al., 2022).

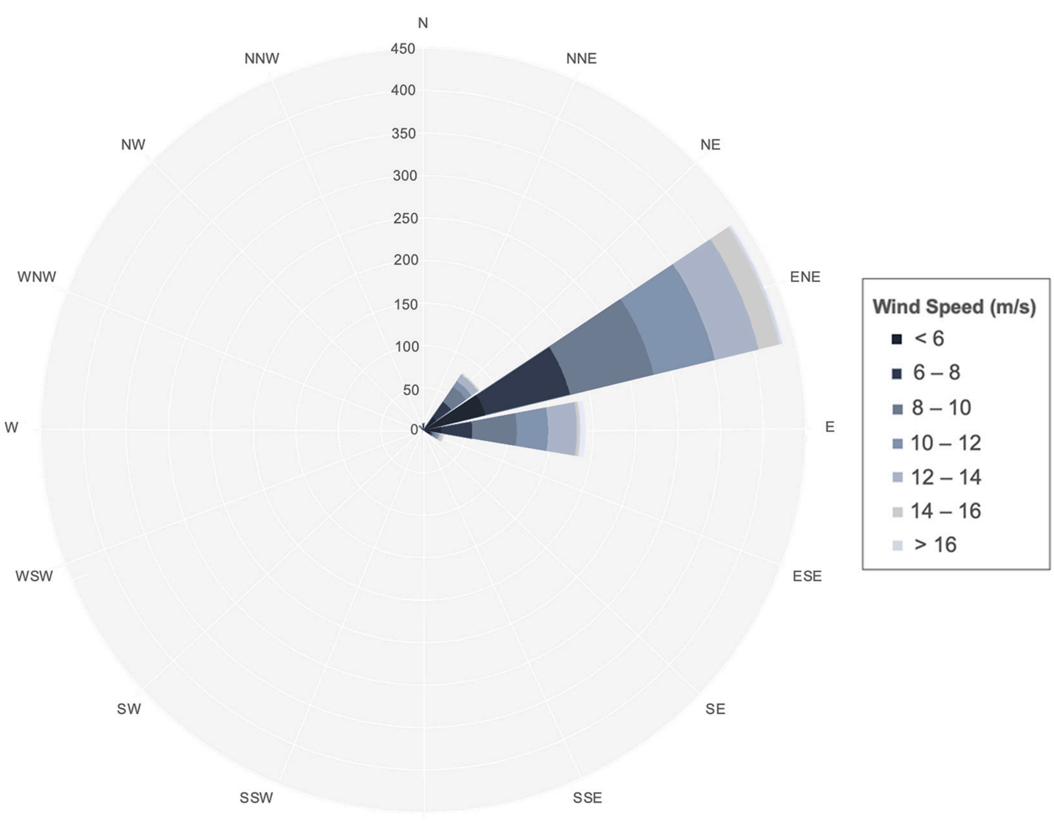

Fig. 5. ERA5-Land 10 m wind speeds and directions associated with the activation of dust plume events at Etosha Pan from 2000 to 2022 (n = 785).

Although dust plume events were observed to occur across a wide range of measured wind speeds each year, thresholds for erosion were notably lower (<6 up to 8 m s^{-1}) for a greater proportion of dust plume events recorded during the dry and highly emissive years of 2015, 2016 and 2019. These results closely correspond to the measured modal threshold for dust emission at wind speeds of c. 7.25 m s^{-1} (at 3.18 m height) identified from ground-based observations by Wiggs et al. (2022) between July 2015 and June 2016.

Fig. 6 shows the 2000–2022 ERA5-Land daily 10 m wind speeds (Fig. 6a) and wind gusts (Fig. 6b), binned and plotted as relative frequencies for the active dust season (i.e., the period from May to October where greater dust emission activity was observed [see Fig. 3]) over Etosha Pan. Dust days are binned according to the corresponding ERA5-Land average wind speeds and gusts for each dust day and plotted as a relative frequency in each graph, respectively.

Shown in Fig. 6a, the observed dust emission days were associated with higher wind speeds, and typically peaked at daily mean wind speeds of 6 m s^{-1} to 7 m s^{-1}. Correspondingly, mean daily DOD measured over the Etosha region was found to be significantly correlated with ERA5-Land daily mean wind speeds ($r = 0.48$, $p < 0.01$). The association was marginally improved when mean wind speeds were cubed (W^3) ($r = 0.50$, $p < 0.01$), in line with previous observations in southern Africa (Bryant et al., 2007). Shown in Fig. 6b, the observed dust emission days also correspond with periods of higher ERA5-Land daily mean wind gusts, which typically peaked at 8 m s^{-1} to 9 m s^{-1}. A significant and slightly improved correlation was also found between mean daily DOD values and ERA5-Land wind gusts ($r = 0.49$, $p < 0.01$) compared with wind speeds over the Etosha region during the analysis period. Research by Engelstaedter and Washington (2007a, 2007b) similarly found improved agreement between ERA-40 wind gust data and dust emissions in North Africa, attributed to the importance of turbulence and near surface convergence on dust uplift related to the breakdown of nocturnal low-level jets (LLJs) for morning emission events during winter months and cold pool outflows from convective storms for afternoon emission events during summer. Indeed, recent field-based studies at Etosha Pan have established similar links between dust emission dynamics associated with turbulent, gusty winds driven by LLJ activity in the austral winter and convective storm activity in the austral summer (Clements and Washington, 2021; Wiggs et al., 2022).

4.3. Surface hydrology

Mean annual precipitation estimates derived from satellite gridded precipitation products (TRMM/GPM-IMERG) show a rainfall gradient across the Cuvelai-Etosha Basin, ranging from ~700 to 820 mm yr^{-1} in the northeastern part to ~240–300 mm yr^{-1} in the southwest (Fig. 7).

Inter-annual variations in MODIS lake surface inundation extents and flooding frequencies at Etosha Pan displayed in Fig. 8 align with observed rainfall patterns in the Cuvelai-Etosha Basin. The most frequent and extensive flooding of the pan surface was observed during hydrological years (July–June) from 2008 to 2012 (Fig. 8), which corresponded with periods of above average rainfall in the region (up to 811 mm recorded in 2009). However, mean lake surface inundation extents and flooding frequencies did not necessarily show close agreement. Greater average inundation extents were recorded in 2008 (1725 km^2; 35.9 % of total pan area), reaching a peak in 2009 (2354 km^2; 49 % of total pan area), and 2011 (1378 km^2; 28.7 % of total pan area). While annual flooding durations indicate that Etosha Pan was most frequently flooded in 2009 (265 days; 72.6 % of the hydrological year), 2010 (322 days; 88.2 % of the hydrological year), and 2012 (357 days; 97.5 % of the hydrological year) (Fig. 8). This suggests that extensive inundation of the pan surface is not always synonymous with prolonged flooding periods, where periods of frequent flooding did not necessarily generate the largest areal extents of pan surface inundation, and the most extensive flooding events were not necessarily the most frequent or prolonged in duration. Furthermore, it was during the wettest hydrological years between 2008 and 2012 that the greatest variability in pan surface flooding extent (±1 standard deviation) was observed (Fig. 8). At the individual flooding event scale, inundation of the pan surface varied across much smaller and larger extents than mean values suggest. For example, pan surface inundation areas fluctuated considerably around the annual average (1378 km^2; 28.7 % of total pan area) in 2011, ranging from 9.2 km^2 (0.2 % total pan area) up to 4051 km^2 (84.3 % total pan area) for discrete ephemeral flooding events.

Both the annual lake surface inundation extents and flooding occurrences were consistently lower for the hydrological years of 2015 (40.7 km^2; 14 days flooded), 2016 (58.2 km^2; 27 days flooded), and 2019 (17.3 km^2; 9 days flooded) (Fig. 8). These observations are consistent with records of below average catchment-scale precipitation for corresponding 'dry' years (as low as 379 mm recorded in 2019), which have been noted for causing some of the most extreme droughts in Namibia in the last century (Liu and Zhou, 2021). It is likely that such dry conditions on the pan surface and in the surrounding catchment contributed to the measured increase in atmospheric mineral dust (DOD) and the high frequencies of dust plume events and dust day occurrences recorded from Etosha Pan in these years (Fig. 2).

Fig. 9 shows the seasonal variabilities of satellite-retrieved mean monthly precipitation totals in the Cuvelai-Etosha Basin and lake surface inundation extents at Etosha Pan from 2000 to 2022. The catchment-scale wet and dry seasons are clearly divisible, with periods of increased rainfall in the catchment recorded during the austral summer wet season (November–April) which decline into the austral winter dry

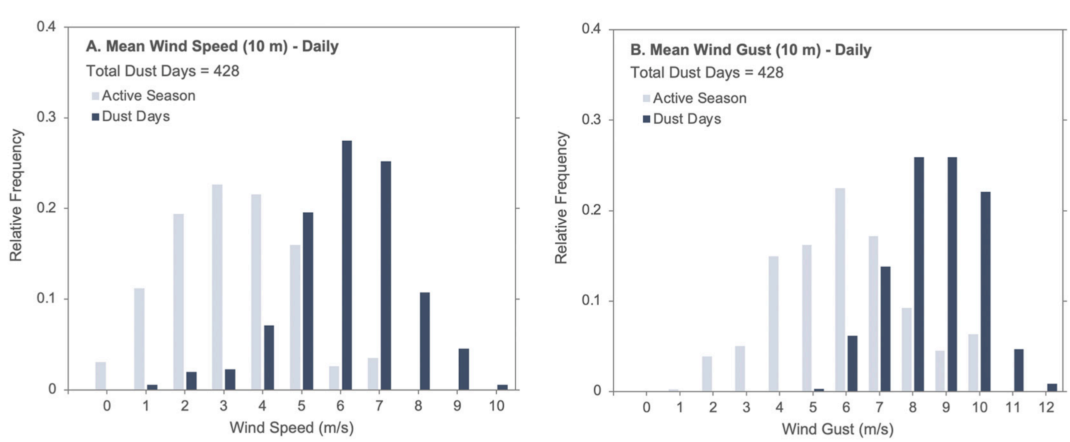

Fig. 6. Frequency distributions of ERA5-Land (a) daily mean wind speeds and (b) daily mean wind gusts associated with the active dust emission season (May to October) (grey) and for dust days only (dark blue) plotted as a function of relative wind speed frequency.

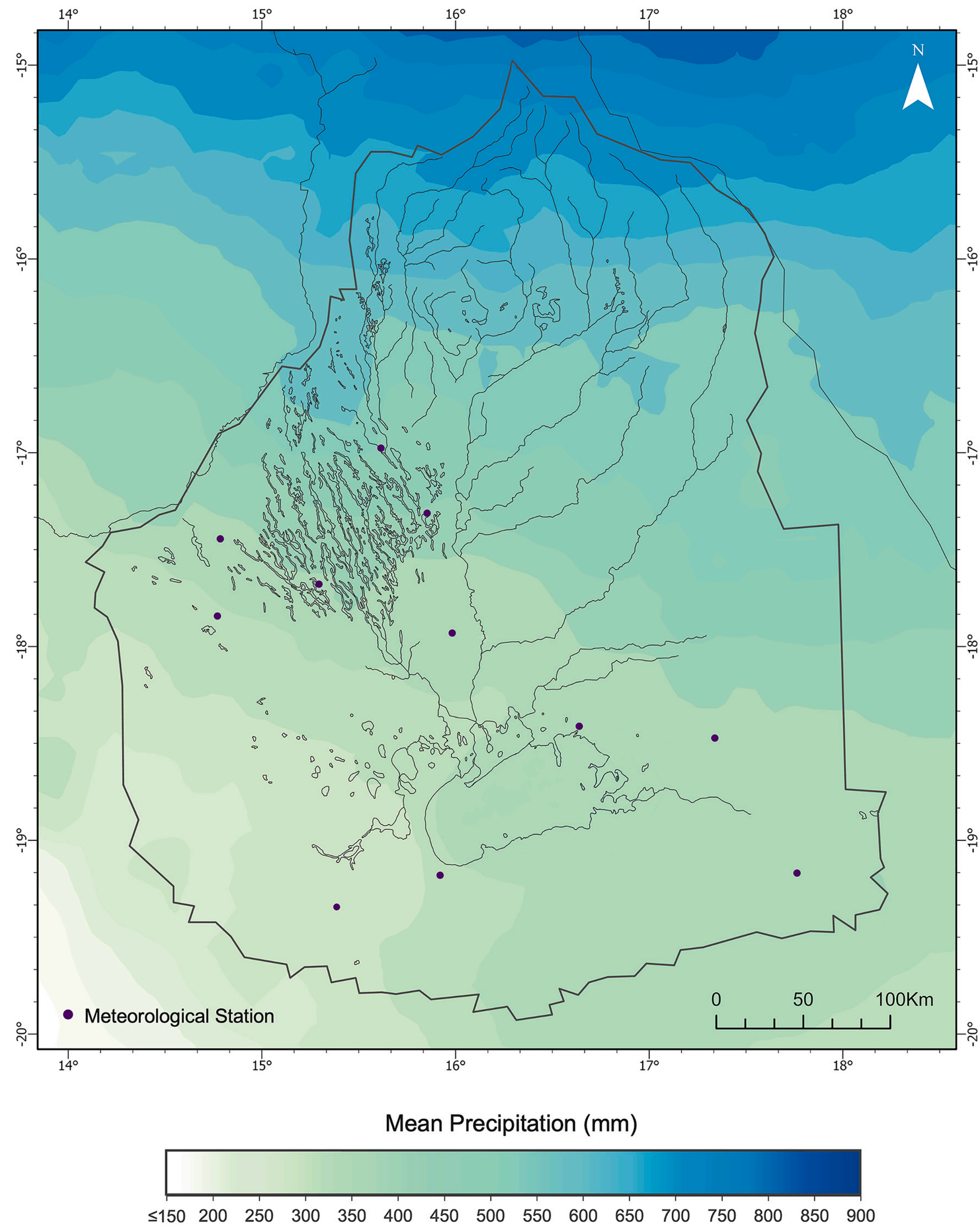

Fig. 7. Spatial distribution of mean annual precipitation (572 mm yr^{-1}) in the Cuvelai-Etosha Basin from 2000 to 2022. The contour map shows that mean annual precipitation decreases along a NE–SW gradient. Purple points indicate the principal meteorological stations utilised in this study.

season (May–October). Mean monthly rainfall totals were highest and showed the greatest inter-annual variability during the wettest months of January (132.82 mm ± 47.39 mm), February (125.39 mm ± 47.79 mm) and March (119.65 mm ± 28.78 mm) (Fig. 9). In contrast, mean precipitation was lowest and showed the least inter-annual variability in the months of June (0.49 mm ± 0.88 mm), July (0.07 mm ± 0.10 mm), and August (0.35 mm ± 0.33 mm) in the dry season (Fig. 9).

Pan surface inundation demonstrated a lagged response to seasonal catchment rainfall variability for the 2000–2022 period. Average monthly inundation extents generally increased one to two months following periods of extensive rainfall during the austral summer wet season (November–April), reaching peak values in the months of March (1094 km^2), April (1052 km^2) and May (974 km^2) following periods of extensive rainfall in January and February (Fig. 9). This is followed by a decline throughout the dry season in the months of June to October, with the lowest average inundation extents observed at the start of the wet season in November (365 km^2) and December (371 km^2), respectively (Fig. 9). The variability in wet/dry season rainfall in the Cuvelai-Etosha Basin is also reflected in inherent fluctuations in flooding extent at Etosha Pan (±1 standard deviation) in Fig. 9, caused by extremes in lake surface inundation that were considerably higher than monthly average values during 2008–2012 and lower than monthly average

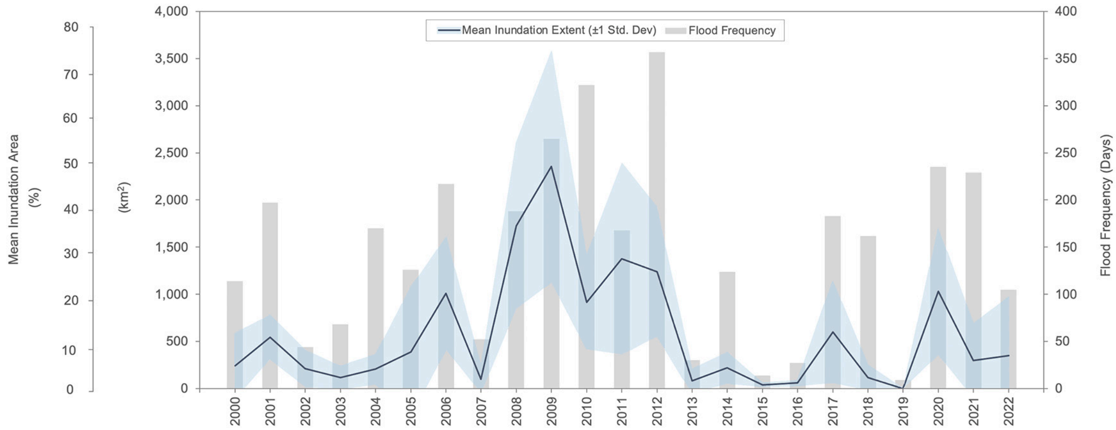

Fig. 8. Annual mean lake surface inundation extents (±1 standard deviation) and total frequency of flooding at Etosha Pan for hydrological years (July–June) from 2000 to 2022.

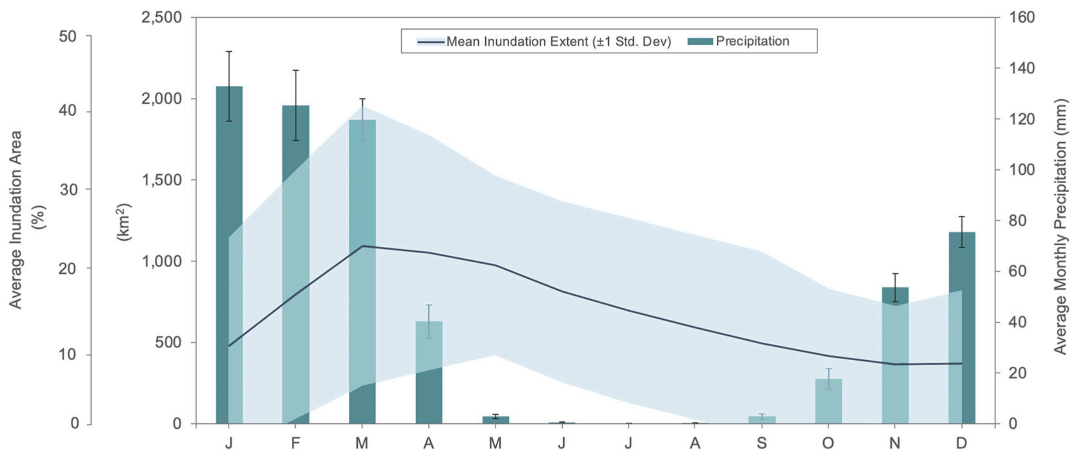

Fig. 9. Mean monthly lake surface inundation extents (±1 standard deviation) at Etosha Pan and mean monthly precipitation totals in the Cuvelai-Etosha Basin (derived from satellite-retrieved [TRMM/GPM-IMERG] gridded precipitation data) from 2000 to 2022.

values during 2015, 2016 and 2019, in accordance with inter-annual trends (Fig. 8).

Spatiotemporal patterns of annual lake surface inundation frequencies and dust plume occurrences at Etosha Pan (Fig. 10) are consistent with observed interannual and seasonal variability in catchment rainfall and flooding within the ephemeral basin, as well as with fluctuations in dust event frequency. Dust plume activity is generally lower during wetter years, characterised by more extensive and frequent flooding of the pan surface, and higher during drier periods. Notably, most dust emission events originated from surfaces that had undergone some degree of inundation or wetting in the year preceding the observed dust activity (Fig. 10), potentially indicating a lagged response between antecedent hydrological conditions and subsequent dust source activation.

A spatial trend in ephemeral flooding dynamics may be also inferred from the annual flooding frequency composites (Fig. 10). Generally, the most frequently flooded pixels are located in a small area in the northwestern region of Etosha Pan, situated south of the Ekuma and Oshigambo Rivers. In the instances where inundation of the pan surface extends beyond this region, floodwaters are channelled in an eastward direction along the northern fringe, accentuating the subtle natural slope of the pan surface where the eastern portion is ~5 m lower in elevation than the west (Mendelsohn et al., 2013). This then coincides with fluvial inlets draining from the Oshangulu River in the north and Owambo River in the east to inundate the eastern portion of Etosha Pan. Where inundation of the pan surface is more extensive, floodwaters generally fill the eastern portion and then spread in a westward direction, principally via a shallow channel running along the southern region of the pan (Fig. 10). These spatial trends are consistent with the northeast to southwest rainfall gradient that exists across the Cuvelai-Etosha Basin (Fig. 7) (Mendelsohn et al., 2013; Hamunyela et al., 2022). Floodwaters from the northern regions of the catchment are thus transported southwards via ephemeral river channels (iishana), which converge into the Ekuma and Oshigambo Rivers that drain into the northwest of Etosha Pan (Bryant, 2003).

Spatiotemporal connections clearly exist between rainfall variability across the Cuvelai-Etosha Basin and surface flooding dynamics at Etosha Pan at both annual and seasonal scales. Pearson correlation analysis (Table 1) reveals significant positive associations between annual catchment-scale precipitation totals and pan surface flooding extents ($r = 0.67$, $p < 0.01$) and frequencies ($r = 0.64$, $p < 0.01$) over the 2000–2022 period, indicating that wetter years are generally associated with more extensive and frequent flooding of the pan surface. At the seasonal scale, moderate but significant correlations were observed between monthly precipitation totals and pan surface flooding with one- to two-month lags, with the strongest correlation coefficients found for two-month lagged extents ($r = 0.42$, $p < 0.01$) and frequencies ($r = 0.44$, $p < 0.01$) (Table 1). These lagged responses align with seasonal catchment-scale precipitation and pan surface flooding dynamics (Fig. 9) and likely reflect delayed hydrological routing through the catchment, as rainfall is progressively conveyed to Etosha Pan via ephemeral river channels.

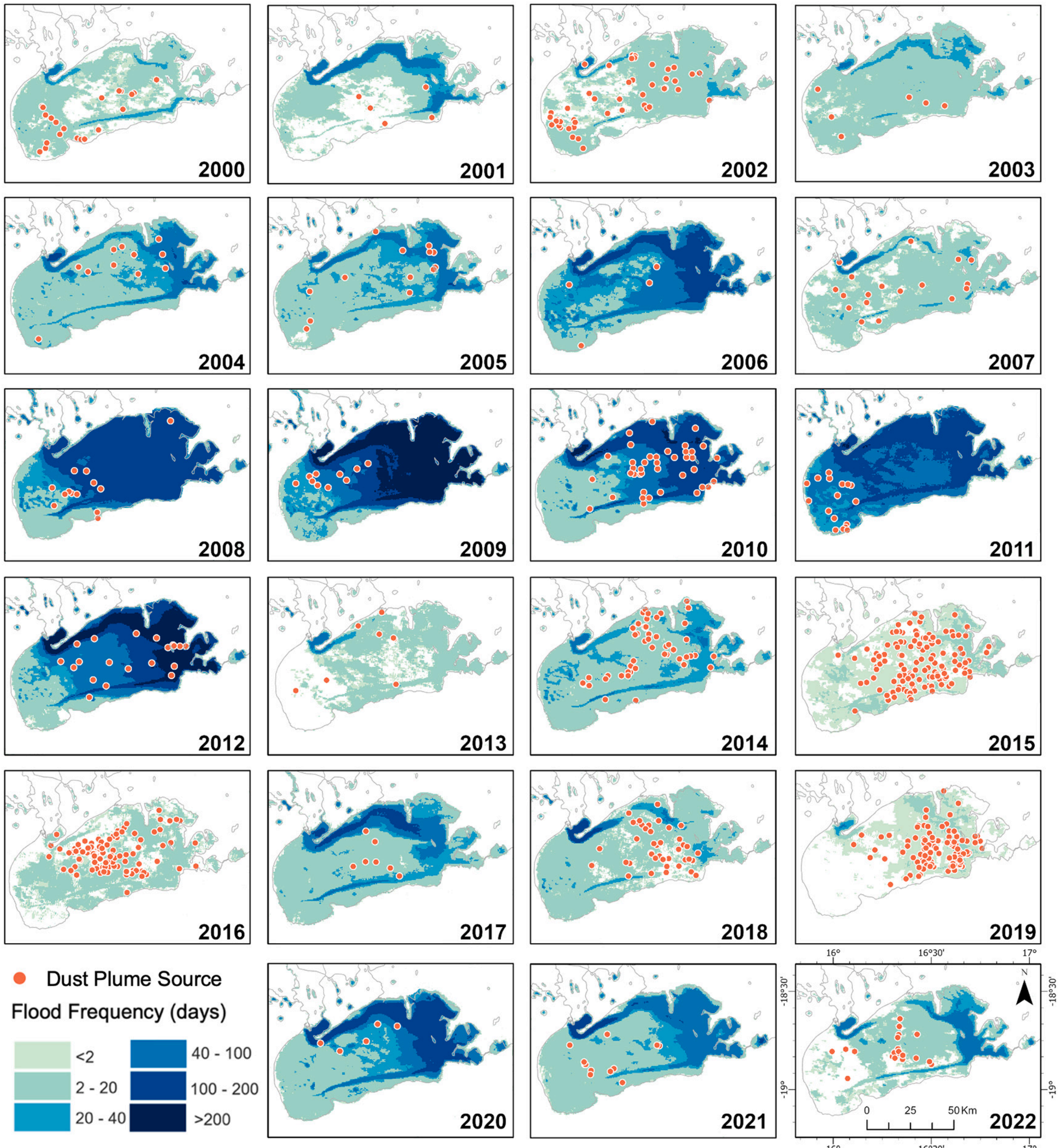

Fig. 10. Spatiotemporal distributions of annual dust emission events (orange points) and lake surface inundation frequencies at Etosha Pan, where the value of each pixel indicates the number of days the pan experienced flooding during the hydrological years (July to June) from 2000 to 2022. Inundation of the pan surface generally follows a consistent pattern: floodwaters primarily enter from the north-west, draining into the pan from the Ekuma and Oshigambo Rivers. These waters then flow eastward along the northern edge, filling the eastern portion of the pan, before spreading westward via a shallow channel along the southern region.

Table 1
Pearson correlation coefficients between satellite-derived catchment precipitation totals in the Cuvelai-Etosha Basin and lake surface inundation extents and frequency of flooding at Etosha Pan across annual, monthly (+1 and +2 month lags), and daily timescales from 2000 to 2022.

Time period	Inundation extent (km^2)	Flood frequency (days)
Annually	0.67**	0.64**
Monthly	0.21	0.094
+1 month lag	0.37*	0.31**
+2 month lag	0.42**	0.44**
Daily	0.047	0.00

* Significant at the 0.05 level.
** Significant at the 0.01 level.

4.4. Establishing the links between global climate drivers, regional hydrology and mineral dust emissions

Our analyses reveal clear relationships and cyclical patterns between interannual and seasonal variations in dust events from Etosha Pan, catchment-scale precipitation, and surface flooding dynamics within the ephemeral basin. We now examine the role of regional and global climate drivers in explaining the variability in dust emissions, which is critical for improving the accuracy of dust emission models. Monthly time-series data presented in Fig. 11 help to elucidate the complex interactions between the observed variables and broader climate systems.

As has been shown above (Figs. 2 and 3), anomalies in MODIS dust optical depth (DOD) and ERA5-Land cubed surface wind speeds (W^3) reveal significant interannual variability in the dust cycle at Etosha Pan (Fig. 11a). Positive and negative anomalies generally coincide with dry and wet phases across the basin. During dry years, particularly from 2000 to 2005, monthly DOD trends show close agreement with mean

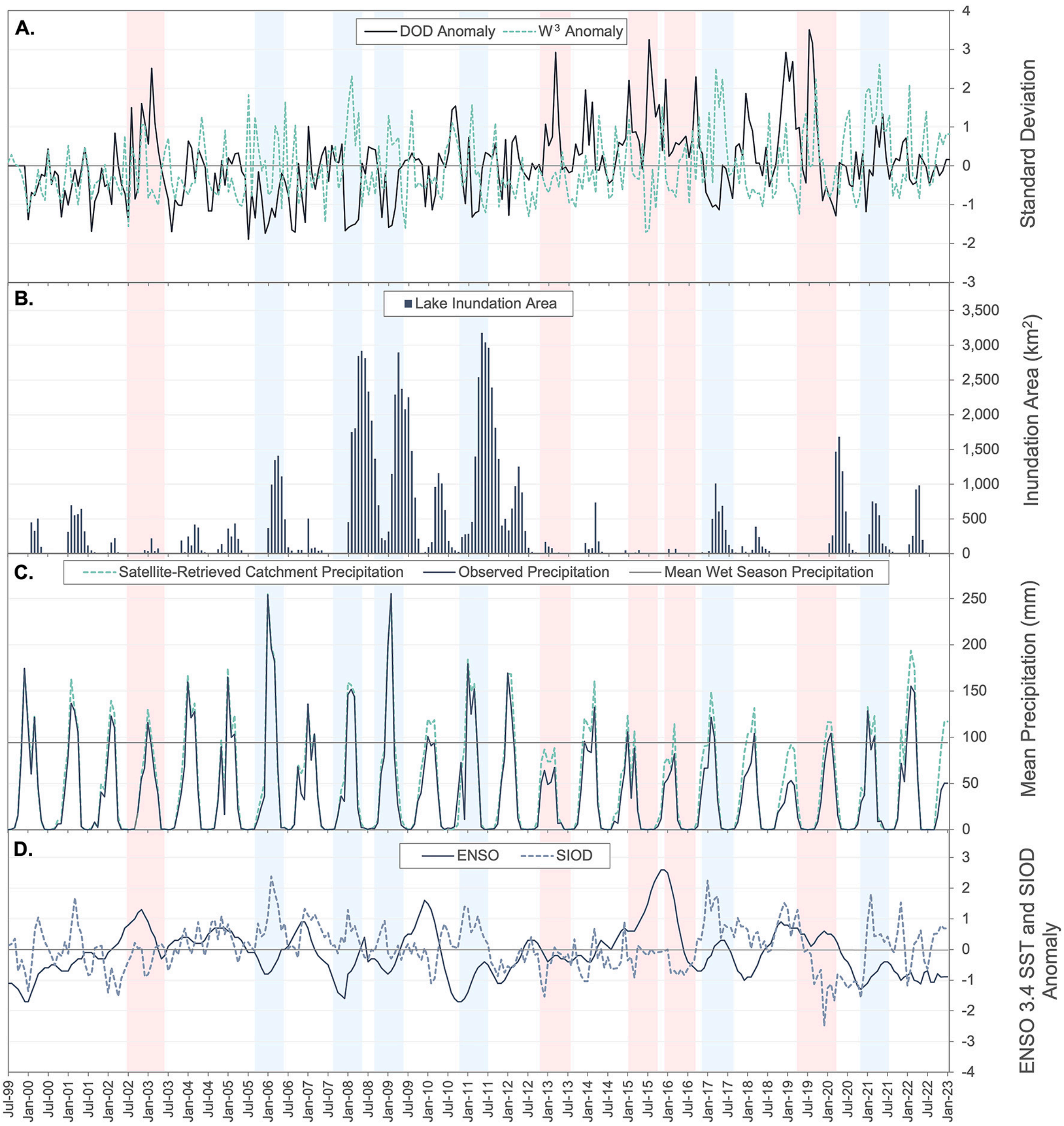

Fig. 11. Monthly time-series from July 1999 to January 2023 showing: (a) MODIS dust optical depth (DOD) and cubed surface wind speed (W^3) anomalies; (b) lake surface inundation extents at Etosha Pan; (c) precipitation totals over the Cuvelai-Etosha Basin, derived from ground-based observations and satellite-retrieved estimates (TRMM/GPM-IMERG); and (d) anomalies in the El Niño-Southern Oscillation (ENSO 3.4 SST) and Subtropical Indian Ocean Dipole (SIOD) indices. Blue shading indicates periods when negative ENSO phases coincide with positive SIOD anomalies, generally associated with increased rainfall in the Cuvelai-Etosha Basin. Red shading indicates periods when positive ENSO phases align with negative SIOD anomalies, typically linked to reduced rainfall in the region.

cubed wind speeds over Etosha Pan. However, this relationship diverges in 2006, when negative DOD anomalies (−2 standard deviations) were recorded despite positive wind speed anomalies of similar magnitude (+2 standard deviations) (Fig. 11a). This decoupling suggests a reduction in dust emissions despite enhanced wind conditions and coincides with major changes in surface hydrology. Between November 2005 and April 2006, the previously mostly dry pan became progressively inundated, reaching an extent of approximately 1500 km^2 (~30 % of the total pan area) (Fig. 11b). This hydrological shift followed a sharp increase in mean monthly catchment precipitation (~250 mm $month^{-1}$) (Fig. 11c), which coincided with a negative ENSO phase (La Niña event) in the tropical Pacific and a positive SIOD phase (Fig. 11d). A similar decoupling between DOD and wind speed anomalies was observed in 2008, 2009, 2011, 2017 and 2020 (Fig. 11a). These years were also characterised by frequent and extensive inundation across Etosha Pan (Fig. 11b), following above average rainfall across the Cuvelai-Etosha Basin (Fig. 11c), which generally corresponded with a negative ENSO phase (La Niña event) and a positive SIOD phase (Fig. 11d). In contrast, significant positive DOD anomalies (+3 standard deviations) were recorded in 2013, 2015, 2016 and 2019 despite negative wind speed anomalies during the same periods (Fig. 11a). These increases in dust emissions occurred during very dry years when pan surface inundation was minimal (<100 km^2 $month^{-1}$) (Fig. 11b), following periods of below average precipitation (<100 mm $month^{-1}$) across the Cuvelai-Etosha Basin (Fig. 11c). These conditions aligned with either a positive ENSO phase (El Niño event), a negative SIOD phase, or both (Fig. 11d).

The time-series data on DOD, surface wind speeds, pan inundation, and catchment-scale precipitation (Figs. 11a–d) collectively indicate a strong linkage between seasonal hydrological variability and dust emission dynamics at Etosha Pan. To quantify these relationships, Pearson correlation analyses were conducted between dust emission indicators (DOD and dust plume frequency) and key hydrological variables, including inundation extent (km^2), flooding frequency (flood days), and catchment-scale precipitation (mm) for the 2000–2022 period (Table 2).

Across annual timescales, significant moderate negative associations were found between both pan surface inundation extents and flooding frequencies with DOD ($r = -0.52$, $p < 0.01$ and $r = -0.39$, $p < 0.01$, respectively) and plume event frequencies ($r = -0.48$, $p < 0.05$ and $r = -0.55$, $p < 0.01$, respectively) (Table 2). This suggests that, as might be expected, dust emission activity at Etosha Pan is significantly reduced during wet years characterised by extensive and frequent inundation of the pan surface. This reflects the immediate influence of floodwater presence on the pan surface inhibiting the availability of sediment from erosion despite the presence of high wind speeds over the region (Bryant, 2003; Mahowald et al., 2003; Bryant et al., 2007). Correspondingly, significant negative associations were found across shorter timescales, between monthly pan surface flooding variables and dust emission activity variables for corresponding months ($r = -0.20$ to -0.31, $p < 0.01$) and between daily observed inundation extents and DOD ($r = -0.19$, $p < 0.05$) (Table 2).

Significant moderate negative associations were also found between catchment precipitation and dust emission variables (DOD and plume event frequencies) across all timescales of interest (Table 2). This further suggests that despite elevated wind speeds, dust emissions were inhibited during and immediately following periods of rainfall. Table 2 shows that the negative associations between catchment precipitation and dust emission variables (DOD and plume event frequencies) were stronger than associations between pan surface flooding and dust emission activity, particularly across shorter-term monthly and daily timescales (Table 2).

Previous research in similar playa sources has shown that changes in soil moisture and salinity in response to both direct precipitation and associated groundwater table fluctuations can alter surface crust stability and the inter-particle cohesive forces that determine surface resistance to aeolian entrainment (Reynolds et al., 2009; Nachshon et al., 2011). Hence, the significant influence of precipitation on inhibiting dust emissions observed in the data presented here likely signifies the effects of rainfall-induced changes in surface moisture and water table levels, which further compound the suppression of dust emissions by periodic inundation. Indeed, the gradual reduction in correlation coefficients as consecutive monthly lags were introduced (Table 2) may reflect the weakening effect of surface water presence and subsurface moisture dynamics on inhibiting sediment availability for erosion as the surface dries out (Mahowald et al., 2003; Reynolds et al., 2007, 2009).

Observations from the data presented here corroborate those of Bryant (2003) and Mahowald et al. (2003), which suggest that rainfall-driven surface flooding dynamics have a significant influence on the timing and magnitude of aeolian dust emissions at Etosha Pan. Bryant (2003) hypothesised that it was through influencing sediment supply dynamics, in which flood events deliver a supply of sediment from ephemeral channel inputs that becomes susceptible to wind erosion in the following dry seasons (with a lag of 1–2 years), that ultimately determines atmospheric dust loadings from the pan surface. The data in the 2000–2022 time-series displayed in Fig. 11 similarly show a notable increase in dust emissions during the dry years of 2013, 2015, 2016 and 2019, which followed particularly wet years of 2006, 2008, 2009, 2011 and 2012 characterised by frequent and extensive surface inundation of the pan. However, correlations between dust emission variables and pan surface flooding and catchment-scale rainfall drivers with annual lags of +1, +2 and +3 years were found not to be significant (Table 2). Nevertheless, Table 2 shows that when a shorter (+3 month) lag was introduced, positive associations were found between monthly pan surface flooding extents with mineral dust DOD ($r = 0.16$, $p < 0.01$) and dust plume event frequencies ($r = 0.14$, $p < 0.05$) as well as between monthly pan surface flooding frequencies and DOD ($r = 0.18$, $p < 0.01$). A significant positive association was also found between monthly catchment precipitation totals and DOD with a +3 month lag ($r = 0.23$, $p < 0.05$) (Table 2). This suggests that ephemeral inundation and (or) wetting of the pan surface by rainfall promoted dust emissions across much shorter seasonal timescales (~3 months) compared with the 1–2 year lags observed in previous studies (Bryant, 2003; Mahowald et al., 2003).

The dust system at Etosha is clearly sensitive and responsive to changes in regional climate and hydrological disturbances. The significant influence of catchment-scale rainfall variability on pan surface inundation and moisture conditions critical for dust emissions underscores the importance of examining potential relationships with regional climate drivers. Shown in Table 3, statistically significant correlations were found over the 2000–2022 period between peak wet season (December–February [DJF]) rainfall anomalies in the Cuvelai-Etosha Basin and sea surface temperature anomalies in the Pacific ENSO 3.4 region ($r = -0.36$, $p < 0.05$) and the subtropical Indian Ocean Dipole (SIOD) ($r = 0.24$, $p < 0.01$). Weaker but significant correlations were also observed between wet season catchment rainfall anomalies and anomaly index values for the same three-month period in the previous year (DJF –1) for SIOD ($r = 0.16$, $p < 0.05$) and the East Indian Ocean (East IO) ($r = -0.12$, $p < 0.01$) (Table 3).

While the observed correlations are moderate to weak in strength, suggesting that additional factors also influence rainfall variability in

Table 2
Pearson correlation coefficients between satellite-derived lake surface inundation extents and frequency of flooding at Etosha Pan, catchment precipitation in the Cuvelai-Etosha Basin, and dust optical depth (DOD) and plume event frequency at Etosha Pan across annual (+1, +2 and +3 year lags), monthly (+1, +2 and +3 month lags), and daily timescales from 2000 to 2022.

Time period	Inundation extent (km^2)		Flood frequency (days)		Catchment precipitation (mm)	
	Dust optical depth (DOD)	Dust event frequency (plume count)	Dust optical depth (DOD)	Dust event frequency (plume count)	Dust optical depth (DOD)	Dust event frequency (plume count)
Annually	−0.52**	−0.48*	−0.39**	−0.55**	−0.56**	−0.46*
+1 year lag	−0.31	0.43	−0.19	−0.25	−0.35	−0.42
+2 year lag	−0.11	−0.14	0.053	−0.098	−0.16	−0.20
+3 year lag	−0.15	−0.28	−0.08	−0.26	−0.44	−0.59
Monthly	−0.22**	−0.26**	−0.20**	−0.31**	−0.57**	−0.40**
+1 month lag	−0.05	−0.22**	−0.03	−0.23**	−0.45**	−0.35**
+2 month lag	0.092	−0.17**	0.098	−0.13*	−0.35**	−0.24**
+3 month lag	0.16**	0.14*	0.18**	0.05	0.23*	−0.085
Daily	−0.19*	−0.042	−0.17	−0.09	−0.31*	−0.24**

* Significant at the 0.05 level.
** Significant at the 0.01 level.

Table 3
Quarterly Pearson correlation coefficients between wet season (DJF) rainfall anomalies in the Cuvelai-Etosha Basin and large-scale climate indices: tropical Pacific El Niño-Southern Oscillation SST (ENSO 3.4), subtropical Indian Ocean Dipole Index (SIOD), Indian Ocean (West IO and East IO), Tropical Southern Atlantic Index (TSA), Multivariate ENSO Index (MEI V2), and Dipole Mode Index (DMI). Correlations are shown for index anomaly values from the previous year (−1), the same year (0), and the following year (+1) relative to the DJF rainfall season. Positive leads (+1) and negative lags (−1) are based on the DJF reference season for each year from 2000 to 2022.

Quarter	Lag/lead year	ENSO 3.4	SIOD	West IO	East IO	TSA	MEI V2	DMI
DJF	−1	−0.23	0.16*	0.22	−0.12**	−0.08	−0.27	0.11
MAM		−0.19	0.20	0.05	−0.25	0.33	−0.33	0.27
JJA		−0.15	0.37	0.02	−0.45	−0.02	−0.26	0.24
SON		−0.12	0.20	−0.15	−0.34	0.14	−0.25	−0.14
DJF	0	−0.36*	0.24**	−0.02	−0.38	−0.04	−0.40	−0.25
MAM		−0.34	−0.01	−0.16	−0.13	0.01	−0.36	−0.18
JJA		−0.08	0.15	0.18	0.00	−0.08	−0.12	0.02
SON		0.12	0.05	0.12	0.04	0.07	0.05	−0.07
DJF	+1	−0.34	0.45	0.13	−0.56	0.18	−0.41	−0.21

* Significant at the 0.05 level.
** Significant at the 0.01 level.

the basin, their statistical significance indicates that these large-scale climate drivers still exert a measurable impact on regional precipitation patterns. The negative correlation between wet season (DJF) rainfall and ENSO 3.4 SST anomalies supports previous observations over southern Africa, where drier than average conditions tend to occur during El Niño phases (characterised by positive SST anomalies) and wetter than average conditions are generally associated with La Niña events (characterised by negative SST anomalies) (Reason and Rouault, 2002). Observational and reanalysis studies have attributed such patterns to ENSO forcing an equivalent barotropic Rossby wave over southern Africa, which modifies regional mid-tropospheric vertical motions and precipitation anomalies (Ratnam et al., 2014; Hoell et al., 2015). El Niño (La Niña) is thus associated with high (low) pressure over southern Africa that produces anomalous decreases (increases) in precipitation relative to climatological averages (Bryant et al., 2007; Hoell et al., 2017).

Similarly, the positive correlations observed between wet season rainfall anomalies and the SIOD index during the same and previous year (DJF and DJF –1) (Table 3) reinforce findings from climate observation and modelling studies. These have shown that positive (negative) SIOD events are generally associated with above (below) average wet season rainfall across southern Africa (Bryant et al., 2007; Gaughan et al., 2016).

Collectively, these findings indicate that regional climate cycles, particularly ENSO and SIOD, exert an important though partial influence on rainfall variability within the Cuvelai-Etosha Basin. This has significant implications for surface moisture conditions and groundwater hydrology that control dust emission potential at Etosha Pan. Alongside the statistically significant links between catchment precipitation, pan surface flooding, and dust emission activity, the results suggest a possible regional SST-driven control on both the hydrological and dust cycles in this key source region. Importantly, this builds on existing evidence of regional climate (ENSO and SIOD) and hydrological controls on dust emission processes from other major ephemeral lake sources in southern Africa (Bryant et al., 2007).

5. Conclusion

This study provides a comprehensive assessment of the coupled climatic and hydrological controls on aeolian dust emissions from Etosha Pan, Namibia, a major Southern Hemisphere dust source. By integrating 22 years of satellite observations (MSG-SEVIRI and MODIS), meteorological records and reanalysis data, we demonstrate that the frequency, timing, and magnitude of dust emissions from Etosha Pan are strongly influenced by catchment-scale precipitation, surface inundation, and wind regimes across multiple timescales.

Our findings reveal that annual and interannual variations in dust emissions are predominantly governed by hydrological dynamics within the Cuvelai-Etosha Basin, with catchment-scale precipitation exerting a primary control on sediment availability for deflation. Periods of heavy rainfall and subsequent widespread surface flooding were associated with reductions in dust activity, evidenced by significant negative correlations between catchment precipitation and dust metrics (DOD and event frequency) across daily to annual timescales. These associations were stronger than those between dust emissions and pan surface inundation alone, suggesting that the combined effects of rainfall-induced surface wetting and ephemeral river inputs exert a more immediate and sustained constraint on dust availability than flooding alone. For periods when the pan surface is dry and sediment is available, wind speed variability emerges as the dominant driver of dust emissions. Notably, we also find that recent wetting by precipitation and ephemeral inundation can enhance dust emissions upon surface drying over short seasonal timescales (~3 months), in contrast to longer lag times (1–2 years) suggested in previous studies.

Importantly, we establish that large-scale climate drivers, particularly the El Niño-Southern Oscillation (ENSO) and subtropical Indian Ocean Dipole (SIOD), play a key role in modulating the hydrological regime of the Cuvelai-Etosha Basin and, by extension, dust emissions from Etosha Pan. Positive ENSO (El Niño) and negative SIOD phases were significantly associated with reduced rainfall, diminished pan inundation, and enhanced dust emissions despite relatively low wind speeds, while negative ENSO (La Niña) and positive SIOD phases corresponded with wetter conditions, extensive flooding, and suppressed dust activity.

These findings highlight the need to account for the complex interactions between global climate variability, regional hydrology, and dust emission processes in climate and dust modelling frameworks. By clarifying the drivers of dust variability in Etosha Pan, this study contributes towards improved representation of ephemeral lake systems and Southern Hemisphere dust sources in regional and global models, an essential step for improving projections of atmospheric dust loading under future climate change. The identification of statistically robust links between dust activity and global climate oscillations such as ENSO and SIOD opens the prospect of forecasting dust emission trends based on seasonal and interannual climate predictions. This enhances the potential to integrate ephemeral dust sources into predictive frameworks for global dust loading under evolving climate regimes. Building on this work, future research should prioritise the integration of high-resolution remote sensing, targeted field observations, and regional scale dust modelling to better resolve the spatial and temporal complexity of surface-atmosphere interactions for refining predictions of dust dynamics in ephemeral lake environments.

CRediT authorship contribution statement

Natasha S. Wallum: Writing – review & editing, Writing – original draft, Visualization, Validation, Project administration, Methodology, Investigation, Formal analysis, Data curation, Conceptualization. **Giles F.S. Wiggs:** Writing – review & editing, Supervision, Conceptualization. **Robert G. Bryant:** Writing – review & editing, Supervision, Conceptualization.

Financial support

This work is supported by the Natural Environment Research Council's Doctoral Training Programme (NERC-DTP) funded by the UK Research and Innovation (UKRI) (Grant no. NE/S007474/1/2284931) and Hertford College, University of Oxford.

Declaration of competing interest

The authors declare that they have no conflict of interest.

Acknowledgements

Data used for dust emission detection were sourced from Terra and Aqua satellites MODIS Level 2 surface reflectance and operational aerosol product data acquired from the Atmospheric Archive and Distribution System (LAADS) Distributed Active Archive Center (DAAC) (https://ladsweb.nascom.nasa.gov/) and MSG-SEVIRI data procured from the EUMETSAT Data Store (https://data.eumetsat.int/search?query=). Analysis of MSG-SEVIRI imagery utilised the Clear Sky Differencing (CSD) algorithm developed by Jon Murray and colleagues (doi:https://doi.org/10.1002/2016JD025221). Lake area extent data were derived from MODIS Terra data and verified using Landsat 5 TM and Landsat 8 OLI Level-2 (8-day) image data acquired through the USGS Earth Explorer data portal (www.earthexplorer.com). Precipitation data derived from The Integrated Multi-Satellite Retrievals for GPM (GPM-IMERG) and The Tropical Rainfall Measuring Mission (TRMM) gridded precipitation products available from the Goddard Earth Sciences Data and Information Services Center (http://disc.gsfc.nasa.gov/) were augmented with meteorological station data obtained from the Southern African Science Service Centre for Climate Change and Adaptive Land Management (SASSCAL) (https://sasscal.org/) and continuous rain gauge data at Windpoort provided by Wilferd Versfeld, courtesy of Mikhail G. Sorokin and Brent Holben (NASA). Hydrographic vector shapefiles were obtained from the HydroSHEDS catchment database (https://hydrosheds.org/products/hydrobasins). Geospatial boundary data were obtained from the Namibia Statistics Agency (https://nsa.org.na/). N.S.W. is supported by the Natural Environment Research Council's Doctoral Training Programme (NERC-DTP) studentship funded by the UK Research and Innovation (UKRI) (Grant no. NE/S007474/1/2284931) and Hertford College, University of Oxford.

Data availability

The data used in this manuscript can be found in the Oxford University Research Archive: https://doi.org/10.5287/ora-korkq2z7n (Wallum, 2025).

References

Banks, J.R., Heinold, B., Schepanski, K., 2022. Impacts of the desiccation of the Aral Sea on the central Asian dust life-cycle. J. Geophys. Res. Atmos. 127 (21). https://doi.org/10.1029/2022JD036618 e2022JD036618.

Bryant, R.G., 2003. Monitoring hydrological controls on dust emissions: preliminary observations from Etosha Pan, Namibia. Geogr. J. 169 (2), 131–141. https://doi.org/10.1111/1475-4959.04977.

Bryant, R.G., Rainey, M.P., 2002. Investigation of flood inundation on playas within the zone of Chotts, using a time-series of AVHRR. Remote Sens. Environ. 82 (2–3), 360–375. https://doi.org/10.1016/S0034-4257(02)00053-6.

Bryant, R.G., Bigg, G.R., Mahowald, N.M., Eckardt, F.D., Ross, S.G., 2007. Dust emission response to climate in southern Africa. J. Geophys. Res. Atmos. 112 (D9). https://doi.org/10.1029/2005JD007025.

Buch, M.W., Rose, D., 1996. Mineralogy and geochemistry of the sediments of the Etosha Pan region in northern Namibia: a reconstruction of the depositional environment. J. Afr. Earth Sci. 22 (3), 355–378. https://doi.org/10.1016/0899-5362(96)00020-6.

Chappell, A., Webb, N.P., Hennen, M., Schepanski, K., Ciais, P., Balkanski, Y., Zender, C. S., Tegen, I., Zeng, Z., Tong, D., Baker, B., 2023. Satellites reveal earth's seasonally shifting dust emission sources. Sci. Total Environ. 883, 163452. https://doi.org/10.1016/j.scitotenv.2023.163452.

Clements, M., Washington, R., 2021. Atmospheric controls on mineral dust emission from the Etosha Pan, Namibia: observations from the CLARIFY-2016 field campaign. J. Geophys. Res. Atmos. 126 (14). https://doi.org/10.1029/2021JD034746 e2021JD034746.

Clements, M., Washington, R., 2023. Summer dust emissions from the Etosha Pan, Namibia: the role of the Namib anabatic-sea breeze system. J. Geophys. Res. Atmos. 128 (6). https://doi.org/10.1029/2022JD036815 e2022JD036815.

Dansie, A.P., Thomas, D.S., Wiggs, G.F.S., Baddock, M.C., Ashpole, I., 2022. Plumes and blooms—locally-sourced Fe-rich aeolian mineral dust drives phytoplankton growth off Southwest Africa. Sci. Total Environ. 829, 154562. https://doi.org/10.1016/j.scitotenv.2022.154562.

Engelstaedter, S., Washington, R., 2007a. Atmospheric controls on the annual cycle of north African dust. J. Geophys. Res. Atmos. 112 (D3). https://doi.org/10.1029/2006JD007195.

Engelstaedter, S., Washington, R., 2007b. Temporal controls on global dust emissions: the role of surface gustiness. Geophys. Res. Lett. 34 (15). https://doi.org/10.1029/2007GL029971.

Gadal, C., Delorme, P., Narteau, C., Wiggs, G.F., Baddock, M., Nield, J.M., Claudin, P., 2022. Local wind regime induced by giant linear dunes: comparison of ERA5-land reanalysis with surface measurements. Bound.-Layer Meteorol. 185 (3), 309–332. https://doi.org/10.1007/s10546-022-00733-6.

Gaughan, A.E., Staub, C.G., Hoell, A., Weaver, A., Waylen, P.R., 2016. Inter- and intra-annual precipitation variability and associated relationships to ENSO and the IOD in southern Africa. Int. J. Climatol. 36 (4), 1643–1656. https://doi.org/10.1002/joc.4448.

Ginoux, P., Garbuzov, D., Hsu, N.C., 2010. Identification of anthropogenic and natural dust sources using moderate resolution imaging Spectroradiometer (MODIS) deep blue level 2 data. J. Geophys. Res. Atmos. 115 (D5). https://doi.org/10.1029/2009JD012398.

Ginoux, P., Prospero, J.M., Gill, T.E., Hsu, N.C., Zhao, M., 2012. Global-scale attribution of anthropogenic and natural dust sources and their emission rates based on MODIS deep blue aerosol products. Rev. Geophys. 50 (3). https://doi.org/10.1029/2012RG000388.

González-Romero, A., González-Flórez, C., Panta, A., Yus-Díez, J., Córdoba, P., Alastuey, A., Moreno, N., Hernández-Chiriboga, M., Kandler, K., Klose, M., Clark, R. N., 2024. Characterization of the particle size distribution, mineralogy, and Fe mode of occurrence of dust-emitting sediments from the Mojave Desert, California, USA. Atmos. Chem. Phys. 24 (16), 9155–9176. https://doi.org/10.5194/acp-24-9155-2024.

Hamunyela, E., Hipondoka, M., Persendt, F., Nghiyalwa, H.S., Thomas, C., Matengu, K., 2022. Spatio-temporal characterization of surface water dynamics with Landsat in endorheic Cuvelai-Etosha Basin (1990–2021). ISPRS J. Photogramm. Remote Sens. 191, 68–84. https://doi.org/10.1016/j.isprsjprs.2022.07.007.

Hoell, A., Funk, C., Magadzire, T., Zinke, J., Husak, G., 2015. El Niño–Southern oscillation diversity and southern Africa teleconnections during austral summer. Clim. Dyn. 45 (5), 1583–1599. https://doi.org/10.1007/s00382-014-2414-z.

Hoell, A., Funk, C., Zinke, J., Harrison, L., 2017. Modulation of the southern Africa precipitation response to the El Niño-southern oscillation by the subtropical Indian Ocean dipole. Clim. Dyn. 48 (7), 2529–2540. https://doi.org/10.1007/s00382-016-3220-6.

Hsu, N.C., Tsay, S.C., King, M.D., Herman, J.R., 2004. Aerosol properties over bright-reflecting source regions. IEEE Trans. Geosci. Remote Sens. 42 (3), 557–569. https://doi.org/10.1109/TGRS.2004.824067.

Hsu, N.C., Jeong, M.-J., Bettenhausen, C., Sayer, A.M., Hansell, R., Seftor, C.S., Huang, J., Tsay, S.C., 2013. Enhanced deep blue aerosol retrieval algorithm: the second generation. J. Geophys. Res. Atmos. 118, 9296–9315. https://doi.org/10.1002/jgrd.50712.

Kok, J.F., Ward, D.S., Mahowald, N.M., Evan, A.T., 2018. Global and regional importance of the direct dust-climate feedback. Nat. Commun. 9 (1), 1–11. https://doi.org/10.1038/s41467-017-02620-y.

Kok, J.F., Storelvmo, T., Karydis, V.A., Adebiyi, A.A., Mahowald, N.M., Evan, A.T., He, C., Leung, D.M., 2023. Mineral dust aerosol impacts on global climate and climate change. Nat. Rev. Earth Environ. 4 (2), 71–86. https://doi.org/10.1038/s43017-022-00379-5.

Kumar, A., Shukla, G., Singh, A., 2022. Long-range global transport and characterization of dust. In: Singh, R.P. (Ed.), Asian Atmospheric Pollution. Elsevier, Amsterdam, Netherlands, pp. 483–504. https://doi.org/10.1016/B978-0-12-816693-2.00012-3.

Lensky, I.M., Rosenfeld, D., 2008. Clouds-aerosols-precipitation satellite analysis tool (CAPSAT). Atmos. Chem. Phys. 8 (22), 6739–6753. https://doi.org/10.5194/acp-8-6739-2008.

Li, Z., Wang, G., Wang, X., Wan, L., Shi, Z., Wanke, H., Uugulu, S., Uahengo, C.I., 2018. Groundwater quality and associated hydrogeochemical processes in Northwest Namibia. J. Geochem. Explor. 186, 202–214. https://doi.org/10.1016/j.gexplo.2017.12.015.

Liu, X., Zhou, J., 2021. Assessment of the continuous extreme drought events in Namibia during the last decade. Water 13 (2942), 1–18. https://doi.org/10.3390/w13202942.

Mahowald, N.M., Bryant, R.G., del Corral, J., Steinberger, L., 2003. Ephemeral lakes and desert dust sources. Geophys. Res. Lett. 30 (2). https://doi.org/10.1029/2002GL016041.

Mahowald, N.M., Jickells, T.D., Baker, A.R., Artaxo, P., Benitez-Nelson, C.R., Bergametti, G., Bond, T.C., Chen, Y., Cohen, D.D., Herut, B., Kubilay, N., 2008. Global distribution of atmospheric phosphorus sources, concentrations and deposition rates, and anthropogenic impacts. Glob. Biogeochem. Cycles 22 (4). https://doi.org/10.1029/2008GB003240.

Mendelsohn, J., Jarvis, A., Robertson, T. (Eds.), 2013. A Profile and Atlas of the Cuvelai-Etosha Basin. Raison & Gondwana Collection, Windhoek, pp. 1–166.

Meng, X., Yao, F., Zhang, J., Liu, Q., Liu, Q., Shi, L., Zhang, D., 2022. Impact of dust deposition on phytoplankton biomass in the northwestern Pacific: a long-term study from 1998 to 2020. Sci. Total Environ. 813, 152536. https://doi.org/10.1016/j.scitotenv.2021.152536.

Muñoz-Sabater, J., Dutra, E., Agustí-Panareda, A., Albergel, C., Arduini, G., Balsamo, G., Boussetta, S., Choulga, M., Harrigan, S., Hersbach, H., Martens, B., 2021. ERA5-land: a state-of-the-art global reanalysis dataset for land applications. Earth Syst. Sci. Data 13 (9), 4349–4383. https://doi.org/10.5194/essd-13-4349-2021.

Murray, J.E., Brindley, H.E., Bryant, R.G., Russell, J.E., Jenkins, K.F., Washington, R., 2016. Enhancing weak transient signals in SEVIRI false color imagery: application to dust source detection in southern Africa. J. Geophys. Res. Atmos. 121 (17), 10199–10219. https://doi.org/10.1002/2016JD025221.

Nachshon, U., Shahraeeni, E., Or, D., Dragila, M., Weisbrod, N., 2011. Infrared thermography of evaporative fluxes and dynamics of salt deposition on heterogeneous porous surfaces. Water Resour. Res. 47 (12). https://doi.org/10.1029/2011WR010776.

Peng, J., Liu, T., Huang, Y., Ling, Y., Li, Z., Bao, A., Chen, X., Kurban, A., De Maeyer, P., 2021. Satellite-based precipitation datasets evaluation using gauge observation and hydrological modeling in a typical arid land watershed of Central Asia. Remote Sens. 13 (2), 221. https://doi.org/10.3390/rs13020221.

Pickford, M., Senut, B., Hipondoka, M., Person, A., Segalen, L., Plet, C., Jousse, H., Mein, P., Guérin, C., Morales, J., Mourer-Chauviré, C., 2009. Mio-plio-pleistocene geology and palaeobiology of Etosha Pan, Namibia. Commun. Geol. Surv. Namibia 14, 95–139.

Pradhan, R.K., Markonis, Y., Godoy, M.R.V., Villalba-Pradas, A., Andreadis, K.M., Nikolopoulos, E.I., Papalexiou, S.M., Rahim, A., Tapiador, F.J., Hanel, M., 2022. Review of GPM IMERG performance: a global perspective. Remote Sens. Environ. 268, 112754. https://doi.org/10.1016/j.rse.2021.112754.

Prospero, J.M., Ginoux, P., Torres, O., Nicholson, S.E., Gill, T.E., 2002. Environmental characterization of global sources of atmospheric soil dust identified with the Nimbus 7 Total ozone mapping spectrometer (TOMS) absorbing aerosol product. Rev. Geophys. 40 (1), 2-1–2-31. https://doi.org/10.1029/2000RG000095.

Prospero, J.M., Delany, A.C., Delany, A.C., Carlson, T.N., 2021. The discovery of African dust transport to the Western hemisphere and the Saharan air layer: a history. Bull. Am. Meteorol. Soc. 1–53. https://doi.org/10.1175/BAMS-D-19-0309.1.

Pu, B., Ginoux, P., 2016. The impact of the Pacific decadal oscillation on springtime dust activity in Syria. Atmos. Chem. Phys. 16 (21), 13431–13448. https://doi.org/10.5194/acp-16-13431-2016.

Rahm, L., Buch, M., 1997. Groundwater flow in the southern part of the Etosha basin indicated by the chemical composition of water. Madoqua 1997 (1), 129–135.

Ratnam, J.V., Behera, S.K., Masumoto, Y., Yamagata, T., 2014. Remote effects of El Niño and Modoki events on the austral summer precipitation of southern Africa. J. Clim. 27 (10), 3802–3815. https://doi.org/10.1175/JCLI-D-13-00431.1.

Reason, C.J.C., Rouault, M., 2002. ENSO-like decadal variability and south African rainfall. Geophys. Res. Lett. 29 (13), 1638. https://doi.org/10.1029/2002GL014663.

Reynolds, R.L., Yount, J.C., Reheis, M., Goldstein, H., Chavez Jr., P., Fulton, R., Whitney, J., Fuller, C., Forester, R.M., 2007. Dust emission from wet and dry playas in the Mojave Desert, USA. Earth Surf. Process. Landf. 32 (12), 1811–1827. https://doi.org/10.1002/esp.1515.

Reynolds, R.L., Bogle, R., Vogel, J., Goldstein, H., Yount, J., 2009. Dust emission at Franklin Lake playa, Mojave Desert (USA): response to meteorological and hydrologic changes 2005–2008. Nat. Resour. Environ. Iss. 15 (18), 105–115. https://digitalcommons.usu.edu/nrei/vol15/iss1/18.

Schepanski, K., Tegen, I., Laurent, B., Heinold, B., Macke, A., 2007. A new Saharan dust source activation frequency map derived from MSG-SEVIRI IR-channels. Geophys. Res. Lett. 34 (18). https://doi.org/10.1029/2007GL030168.

Tong, D.Q., Gill, T.E., Sprigg, W.A., Van Pelt, R.S., Baklanov, A.A., Barker, B.M., Bell, J. E., Castillo, J., Gassó, S., Gaston, C.J., Griffin, D.W., 2023. Health and safety effects of airborne soil dust in the Americas and beyond. Rev. Geophys. 61 (2). https://doi.org/10.1029/2021RG000763 e2021RG000763.

Vickery, K.J., Eckardt, F.D., Bryant, R.G., 2013. A sub-basin scale dust plume source frequency inventory for southern Africa, 2005–2008. Geophys. Res. Lett. 40 (19), 5274–5279. https://doi.org/10.1002/grl.50968.

Washington, R., Todd, M., Middleton, N.J., Goudie, A.S., 2003. Dust-storm source areas determined by the total ozone monitoring spectrometer and surface observations. Ann. Am. Assoc. Geogr. 93 (2), 297–313. https://doi.org/10.1111/1467-8306.9302003.

Wiggs, G.F.S., Baddock, M.C., Thomas, D.S.G., Washington, R., Nield, J.M., Engelstaedter, S., Bryant, R.G., Eckardt, F.D., von Holdt, J.R.C., Kötting, S., 2022. Quantifying mechanisms of aeolian dust emission: field measurements at Etosha Pan, Namibia. J. Geophys. Res. Earth Surf. 127 (8). https://doi.org/10.1029/2022JF006675 e2022JF006675.

Zhao, A., Ryder, C.L., Wilcox, L.J., 2022. How well do the CMIP6 models simulate dust aerosols? Atmos. Chem. Phys. 22 (3), 2095–2119. https://doi.org/10.5194/acp-22-2095-2022.